



Enhanced Photocatalytic Degradation of Synthetic Dyes and Industrial Dye Wastewater by Hydrothermally Synthesized G–CuO–Co₃O₄ Hybrid Nanocomposites Under Visible Light Irradiation

Shanmugam Mahalingam¹ · Jayavel Ramasamy² · Young-Ho Ahn¹

Received: 6 November 2017 / Published online: 23 December 2017
© Springer Science+Business Media, LLC, part of Springer Nature 2017

Abstract

To enhance the degradation of colour and chemical oxygen demand using photocatalytic activity, Graphene–CuO–Co₃O₄ hybrid nanocomposites were synthesized using an in situ surfactant free facile hydrothermal method. The photocatalytic degradation of synthetic anionic dyes, methyl orange (MO) and Congo red (CR), and industrial textile wastewater dyes under visible light irradiation was evaluated. The synthesized nanocomposite was characterized structurally and morphologically using X-ray diffraction, scanning electron microscopy, X-ray photoelectron spectroscopy, Raman spectroscopy, high-resolution transmission electron microscope, and Fourier transform infrared spectroscopy. Evaluation of the colour indicated complete removal at 15 min of irradiation for the MO and CR dyes, with 99% degradation efficiency. The reaction time for the primary effluent wastewater dye was 60 min for 81% dye removal. In contrast, a longer reaction time was required to meet the national discharge regulation for the raw wastewater dye, 300 min for 60% dye removal. The mechanism for dye degradation using the Graphene–CuO–Co₃O₄ hybrid nanocomposite was elucidated using the Langmuir–Hinshelwood model, and the rate constant and half-life of the degradation process were calculated. The results demonstrate that photocatalytic degradation using a hybrid nanocomposite and visible light irradiation is a sustainable alternative technology for removing colour from wastewater dye.

Keywords Surfactant free synthesized · Graphene–CuO–Co₃O₄ hybrid nanocomposite · Photocatalytic activity · Colour · COD · Visible light irradiation

Introduction

Textile manufacturing in the oldest industry worldwide, and has many unique features. One is water consumption; textiles commonly use 200 L of water to produce 1 kg of product [28]. Commonly, organic chemicals are the primary wastewater contaminants, and have been the subject

of much research. One way to assess the magnitude of the contamination, and wastewater quality, is with the chemical oxygen demand (COD), which measures the total chemical load wastewater that can be oxidized [21, 35]. Many countries have strict regulations on the release of textile industry wastewater with high concentrations of colour and COD. These regulations are because industrial wastewater contains high concentrations of dye materials, chemical oxygen demand, biochemical oxygen demand, total dissolved solids, sodium, chloride, sulphate, hardness, heavy metals, and carcinogenic dye elements [51]. Textile wastewater from dyeing and finishing processes has been a hazardous ecological problem for years [9]. High strength wastewater is characterized as having high COD (> 1600 mg/L) and a strong dark colour [23].

In addition, textile wastewater generally has low BOD to COD ratios (< 0.1), indicating their non-biodegradable nature [4]. This wastewater is typically treated using

✉ Jayavel Ramasamy
rjvel@annauniv.edu

✉ Young-Ho Ahn
yhahn@ynu.ac.kr

¹ Department of Civil Engineering, Disasters Prevention Research Institute, Yeungnam University, Gyeongsan 38541, Republic of Korea

² Centre for Nanoscience and Technology, Anna University, Chennai, Tamil Nadu 600 025, India

conventional techniques, such as biological oxidation [1, 9], chemical coagulation, and activated carbon adsorption [9]. However, these conventional techniques often cannot reach sufficiently low concentrations or have disadvantages connected to cost, efficiency, and sludge generation [1]. Conventional techniques have overcome some limitations by employing advanced oxidation processes (AOPs). The AOPs is a favourable technique, because it produces hydroxyl radicals (OH^\cdot) that are an effective method for degrading dyes and refractory contaminants [15, 37]. The hydroxyl radical is nonselective and a very powerful oxidant; it has a rate constant with organic materials within the range of 10^{-9} – $10^{-10} \text{ M}^{-1} \text{ S}^{-1}$ [16, 22, 42]).

Novel energy sources that are clean, renewable, and alternative to fossil fuels are being actively studied. The most abundant natural energy resource is our natural sunlight energy [38, 39]. This resource has also been adopted for addressing contamination, and one method is heterogeneous photocatalysis. This method has been confirmed as effective for removing hazardous pollutants from aqueous solutions and gaseous media [19].

Successful photocatalytic dye degradation requires generating electron–hole pairs and achieving good electron–hole separation [61, 63]. Although a number of materials have been studied for semiconductor photocatalysis in recent years, improving the efficiency of photocatalysts via doping, nanocomposite, and nano-hybrid materials is an active area of research [26]. An innovative method for improving the energy efficiency of a photocatalyst is through creating hybrid nanocomposite structures that incorporate a carbon material in the semiconducting material [29]. Furthermore, recent work indicates that incorporating carbon materials in advanced photocatalytic applications is significant. Several carbon materials have been used to increase photocatalytic effectiveness, including activated carbon, carbon nanomaterials, carbon onions, carbon dots, graphene oxide, and graphene [36, 56]. Particularly, graphene oxide and graphene are attractive due to their sheet like morphology, and capability of adhering to semiconducting nanomaterial on its basal plane, which blocks aggregation and inhibits electron–hole pair recombination [5, 18]. A wide variety of graphene-based hybrid nanocomposite photocatalytic materials, such as graphene– TiO_2 , graphene– ZnO , graphene– WO_3 , and graphene– CdS , with dissimilar shapes and structures have been studied [8, 54]. The growing demands in the growth of innovative hybrid materials for effective photocatalysis has also encouraged researchers to exploit recently developed 2D carbon allotropes to improve semiconductor photocatalysis.

Visible light sources contain much of the solar spectrum, and great importance has been given to

photocatalytic splitting of water or degradation of organic contamination under visible light irradiation. This is promising for both energy and environmental problems [24, 25, 32]. Hence, two approaches have been developed for visible light driven photocatalysts: (1) modification of TiO_2 [3, 45] and utilization of novel semiconductor materials [27, 50].

Cobalt oxide CoO or Co_3O_4 are p-type semiconductors with exciting electronic and magnetic properties. They have been used in efficient catalytic applications [17], as high temperature solar selective absorbers [6], and pigments for glasses and ceramics [40]. However, cobalt oxides have been rarely considered in photocatalysis research. However, this will likely change as cobalt oxide shows improved photocatalytic activity for CO_2 reduction under visible light, and has been used for oxygen reduction, depollution technologies, and dye-sensitized solar cells for power generation [7, 53]. Development of various metals, e.g. Pt, Ru, Ag, Rh, Au, and Pd [49, 60], and transition metal oxides, such as Co_3O_4 , CoO , Cu_2O and $\alpha\text{-Fe}_2\text{O}_3$ [12, 30, 33], has led to the production of visible light photocatalytic activity in titanium, delay charge carrier recombination, and creation selectivity [58]. CuO is a p-type semiconductor with a narrow band gap of 1.2 eV. CuO has been intensively studied because of its potential applications in photocatalysis, solar cells, magnetic media, semiconductors, field transistors, gas sensors, and Li-ion batteries [10, 47, 57].

In the current study, visible light source was used to study the photocatalytic performance of Graphene– CuO – Co_3O_4 hybrid nanocomposites that were synthesized using an in situ surfactant free hydrothermal method. The hydrothermally synthesized Graphene– CuO – Co_3O_4 hybrid nanocomposites, CuO nanorods, and Co_3O_4 nanoparticles are dispersed and incorporated into a thin and fold-like structure of graphene sheets. The structural morphology and optical properties were studied using various techniques. The photocatalytic dye degradation efficiency was analysed using methyl orange (MO), Congo red (CR), and collected industrial textile effluent and influent dyes under visible light irradiation. The colour, COD, rate constant, and half-life time of the degradation process were calculated. The prepared nanocomposite has higher photocatalytic efficiency, and the visible light irradiation source results shows strong degradation of dye, colour, and COD removal.

The goal of this work was to determine the effectiveness of visible light irradiated photocatalytic degradation on synthetic anionic dyes, i.e., MO and CR, and collected textile industrial dye wastewater, including raw wastewater and primary effluent. We evaluated the effectiveness by studying the effect of visible light irradiation on dye degradation and COD elimination.

Experimental Procedure

Materials and Methods

Graphite powder (99.9%) was obtained from the Kanto Chemical Co. Inc., Japan, extra pure NaNO_3 was obtained from Oriental Chemical Industries, and H_2O_2 (30%) was obtained from Daejung Chemicals & Metals Co., Ltd., Korea. Sulfuric acid (H_2SO_4 , 95%), hydrochloric acid (HCl, 35–37%), and potassium permanganate (KMnO_4 , 99.3%) were supplied by the Duksan Pure Chemicals Co., Ltd., Korea. Hydrazine hydrate (N_2H_4 , 50–60%) was purchased from Sigma-Aldrich Chemical, USA. Extra pure copper (II) chloride dehydrate ($\text{CuCl}_2 \cdot 2\text{H}_2\text{O}$) and cobalt (II) chloride hexahydrate ($\text{CoCl}_2 \cdot 6\text{H}_2\text{O}$) were purchased from the Daejung Chemicals & Metals Co., Ltd., Korea. All chemicals and were used in the purity as received. Laboratory Millipore water was used for required dilutions and rinses.

Synthesized materials were characterized using the following: The XRD patterns were measured using a powder X-ray diffractometer (D8 advance, Bruker, Germany) with $\text{CuK}\alpha$ radiation ($\lambda = 1.5406 \text{ \AA}$) operating at 40 kV and 30 mA. FE-SEM images were obtained using a field-emission scanning electron microscope (S-4200, Hitachi, Japan), and the energy dispersive X-ray spectroscopy (EDX) and elemental mapping, high angle annular dark field –scanning transmission electron microscopy (HAADF-STEM) were obtained using the same instrument. The morphology of the synthesized hybrid nanocomposites was obtained with the HR-TEM, and selected area diffraction (SAED) patterns were collected using an FEI-Tecnai TF-20 operating at an acceleration voltage of 200 kV. The FT-IR spectra were recorded with a Perkin Elmer FT-IR spectrophotometer in the wavenumber range from 400 to 4000 cm^{-1} . XPS analysis were recorded using a Thermo Scientific $\text{K}\alpha$ XPS system (Thermo Fisher Scientific, UK) equipped with a monochromatic Al $\text{K}\alpha$ source with a spot size of 400 μm and pass energy of 30 eV. Raman spectra were analysed using a Raman spectroscopy (HORIBA Jobin-Yvon LabRAM HR, France). We used a PHOTO LAMP (Steel light) SMC 220V-55W E26 5400 K visible light source for photocatalytic irradiation processing. The optical and photocatalytic properties of the synthesized hybrid nanocomposite were studied using an OPTIZEN 3220UV UV-vis spectrophotometer. COD and colour were determined using a COD reactor and direct reading spectrophotometer (DR/2500, HACH, USA).

G-CuO-Co₃O₄ Hybrid Nanocomposite Synthesis

Graphene oxide was synthesized using the modified Hummers method as described in Shanmugam and Jayavel [46]. The G-CuO-Co₃O₄ hybrid nanocomposite was prepared using an in situ surfactant free facile hydrothermal method followed by sonication. This method is simple and cost effective and can be rapidly synthesized. In this method, 100 mg of graphene oxide was suspended in 50 mL of H_2O , and then the solution was ultrasonicated for 2 h. Separately, 100 mg of ($\text{CuCl}_2 \cdot 2\text{H}_2\text{O}$) and 100 mg of ($\text{CoCl}_2 \cdot 6\text{H}_2\text{O}$) were suspended in 25 mL of H_2O and then the solutions were stirred for 2 h. While constantly stirring, 3 M NaOH was added until the solutions reached pH 9. The solutions were subsequently stirred for 2 h. Finally, the solution was transferred to a 150 mL Teflon coated autoclave and 1 ml of hydrogen hydrate was added. The autoclave was placed in a high temperature furnace at 180 °C for 24 h. The autoclave was cooled down to room temperature under ambient conditions. The solution was washed several times with H_2O and ethanol. Finally, the solid product was dried for 24 h at 60 °C to obtain the G-CuO-Co₃O₄ hybrid nanocomposite (Fig. 1).

Photocatalytic Activity, Colour, and COD Removal Using the G-CuO-Co₃O₄ Hybrid Nanocomposite

Because they are common synthetic anionic dyes, MO and CR were selected for the base experiment. Raw dye wastewater (RDW) and primary effluent (PE) were collected from the industrial wastewater treatment plant, Daegu Dyeing Industrial Center (DDIC) Korea. The plant, with a capacity of 85,000 m^3/d , uses three steps to treat wastewater: physical, using a screen and grit chamber; chemical, using neutralization, coagulation, flocculation, and sedimentation; and biological, using activated sludge. Dye wastewater has the following characteristics: pH = 11.5, temperature = 48 °C, biochemical oxygen demand (BOD) = 1050 mg/L, suspended solids (SS) = 63 mg/L, total nitrogen (T-N) = 45 mg/L, total phosphorus (T-P) = 2.5 mg/L, and colour = 1000 unit. The effluent primarily treated by the industrial treatment plant (IWWTP) is discharged to a local municipal wastewater treatment plant (MWWPT) for secondary treatment. The national discharge regulation limits for primary treatment are pH = 7.5, temperature = 37 °C, BOD = 6 mg/L, COD = 47 mg/L, SS = 30 mg/L, T-N = 20 mg/L, T-P = 0.1 mg/L, and colour = 320 unit.

Synthesized G-CuO-Co₃O₄ hybrid nanocomposite, 15 mg, was separately dispersed in 50 mL of MO, CR, effluent, and influent solutions and continuously stirred in a

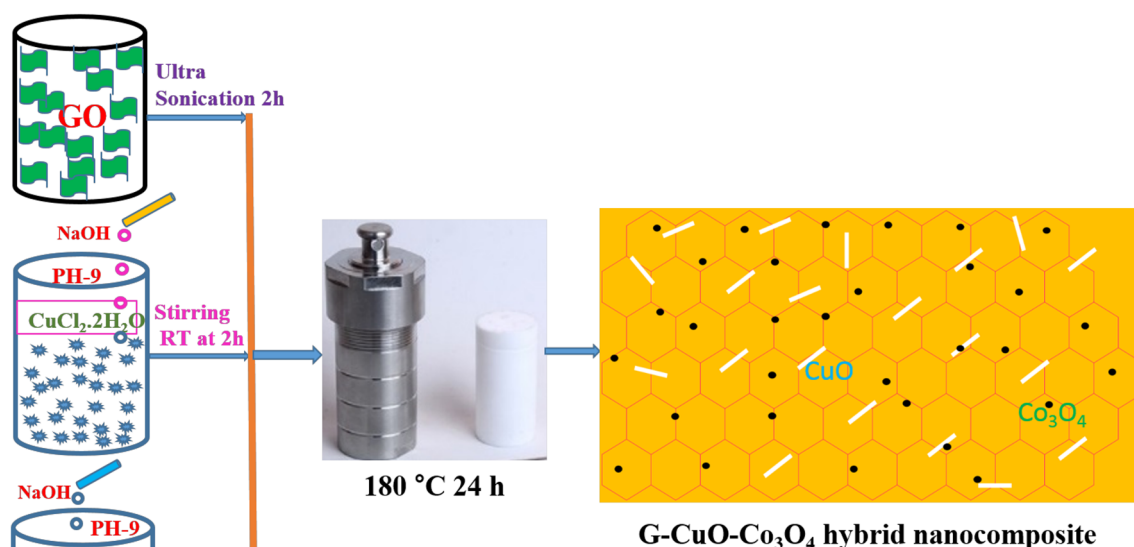


Fig. 1 Schematic showing the synthesis of G-CuO-Co₃O₄ hybrid nanocomposites

dark room for 30 min for adsorption–desorption of the dye molecules. Then, the suspended solution was irradiated with visible light irradiation sources for different time intervals. All experiments were conducted in a similar environment at stable room temperature. Finally, 3 mL visible light irradiated G-CuO-Co₃O₄ hybrid nanocomposite catalyst solutions were examined using the UV–visible spectrophotometers, and the colour and COD values were measured with a COD reactor and direct reading spectrophotometer (DR/2500, HACH, USA). The chemical oxygen demand (COD) values were determined using procedures provided in the American Public Health Association (APHA) handbook [2].

Results and Discussion

Structural Analysis by X-ray Diffractometer

Figure 2 shows the XRD patterns for graphene oxide and the G-CuO-Co₃O₄ hybrid nanocomposite. The XRD pattern for graphene oxide shows two prominent peaks (Fig. 2a) at angles of $2\theta = 10^\circ$ and 42° , which are related to the (002) and (100) planes, respectively. The presence of these peaks confirms the formation of graphene oxide [41]. Figure 2b shows the diffraction pattern of the G-CuO-Co₃O₄ hybrid nanocomposite. A graphene peak is found at a $2\theta = 24.14^\circ$, and the broad angle of the (002) plane of

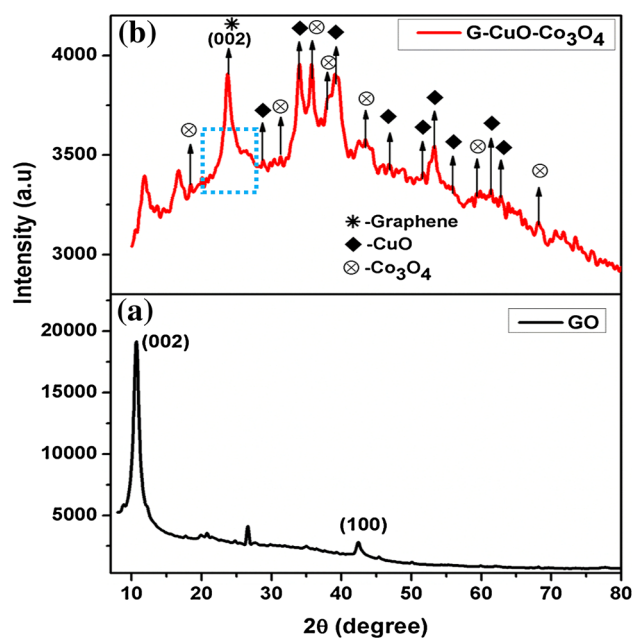


Fig. 2 XRD analyses of a GO, b G-CuO-Co₃O₄ hybrid nanocomposites

hexagonal structured sp^2 bonded carbon is observable. The broad and low intensity peaks in the diffraction pattern of graphene are due to the poor crystalline nature of carbon.

During the hydrothermal process, graphene oxide was reduced to graphene, which provided the broad peak at the 24.14° marked region from the (002) plane of hexagonal

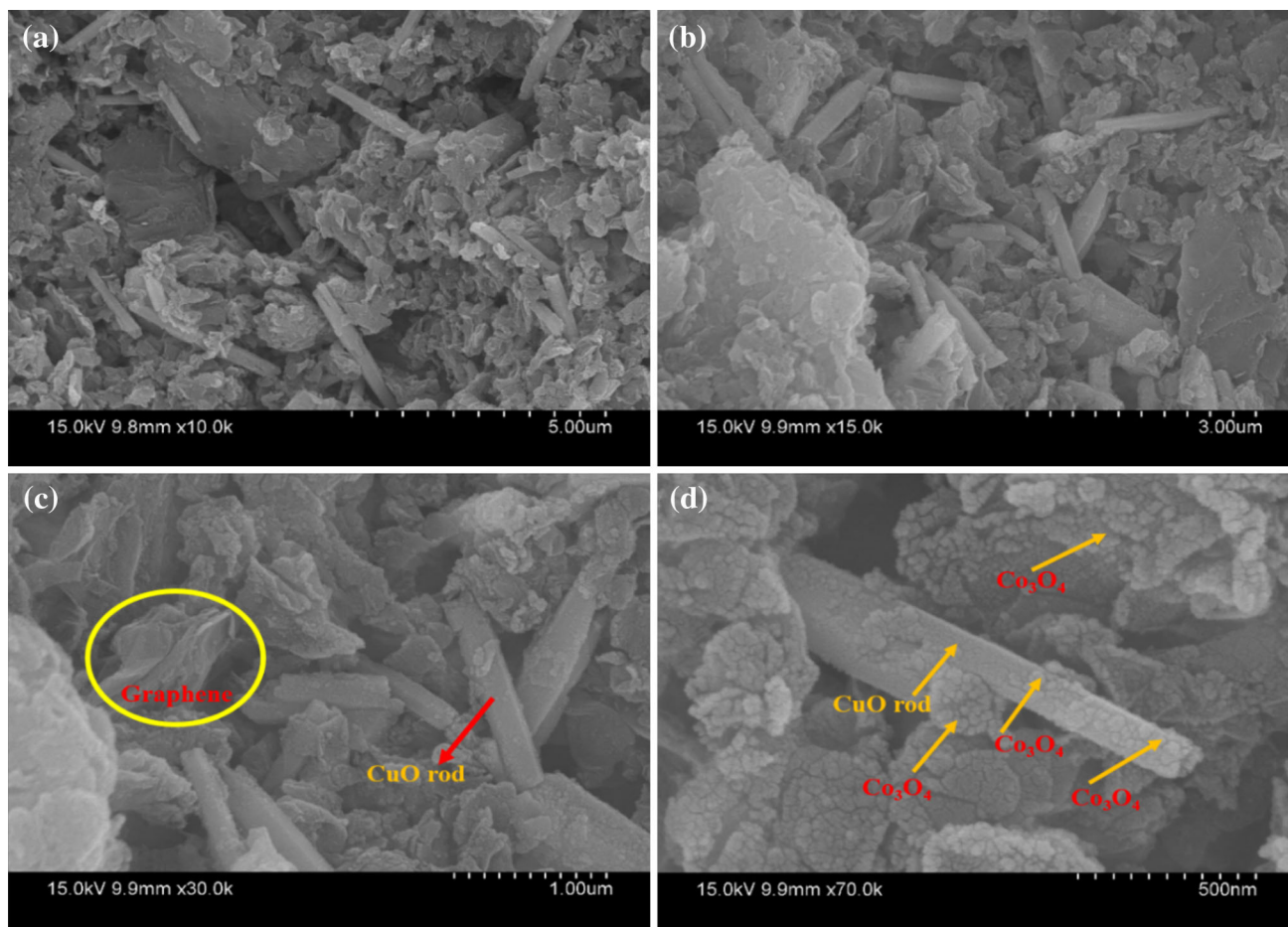


Fig. 3 a–d SEM images of G–CuO–Co₃O₄ hybrid nanocomposites under different magnifications confirming the uniform distribution of the CuO nanorods and Co₃O₄ nanoparticles on the graphene surface

structured sp^2 bonded carbon. The CuO rods at $2\theta = 28.93, 33.96, 39.21, 46.04, 51.74, 53.34, 56.07, 61.31,$ and 62.68 are in agreement with the standard XRD data for the CuO monoclinic phase for an end-centered crystal lattice (JCPDS No. 89-2530, Fig. 2b). The Co₃O₄ nanoparticle crystal structure was characterized using XRD; the peak intensity 2θ value at $18.45, 31.23, 35.79, 38.07, 43.31, 59.49,$ and 65.41 with the standard XRD data values match those in JCPDS No. 073-1701. This clearly shows that Co₃O₄ is a cubic structure [31]. The XRD pattern clearly shows that the CuO nano rods and Co₃O₄ nanoparticles might be uniformly distributed on the graphene sheets or incorporated between the sheets. The XRD results confirmed the formation of G–CuO–Co₃O₄ hybrid nanocomposite.

SEM Morphology Analysis with EDX and Elemental Mapping Analysis

The surface morphology and elemental mapping composition of the synthesized G–CuO–Co₃O₄ hybrid

nanocomposite were studied using FESEM with energy dispersive X-ray (EDX) spectroscopy analysis (Fig. 3). The results indicate that thin and folded structure of graphene, rod-like structure of CuO, and nearly spherical structure of Co₃O₄ nanoparticles are present in the nanocomposites. The higher magnification image, clearly shows nano-sized CuO rods attached to the graphene sheets. The spherical structures of Co₃O₄ nanoparticles are attached to the CuO rods and intercalated between to the graphene sheets (Fig. 3d).

The high annular dark field-scanning transmission electron microscopy (HAADF-STEM) and EDX spectra with elemental mapping of the synthesized G–CuO–Co₃O₄ nanocomposite are shown in Fig. 4. The elemental mapping shows that rich source of carbon (C), oxygen (O), copper (Cu), and cobalt (Co) are present in the nanocomposites. The uniform dispersions of Cu nanorods and Co nanoparticles in the graphene layer, and intercalated between the graphene sheets are clearly shown in Fig. 4b–e. The EDX pattern, Fig. 4f, shows that C, O, Cu, and Co are present in the synthesized G–CuO–Co₃O₄ hybrid

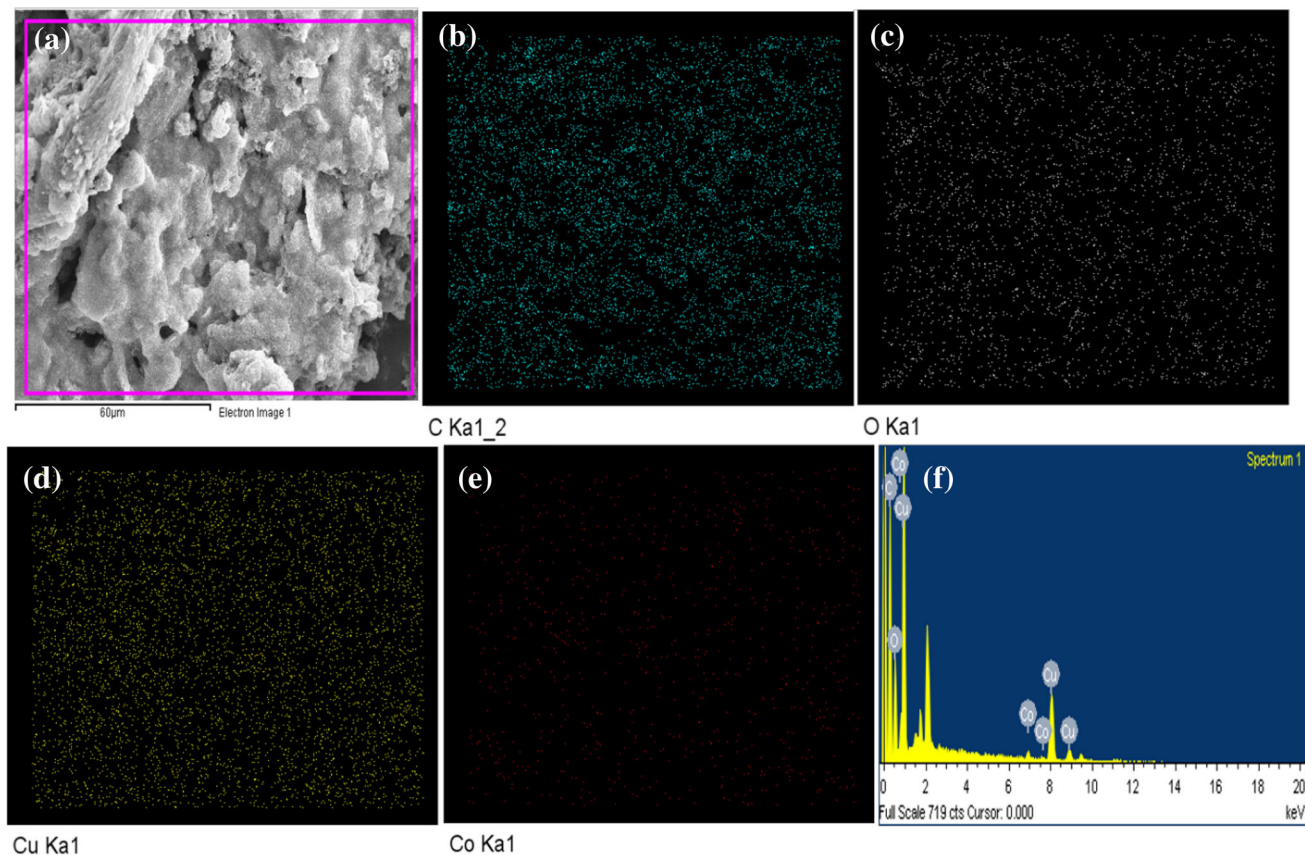


Fig. 4 **a** HAADF-STEM image and corresponding EDX elemental mapping of **b** carbon, **c** oxygen, **d** copper, **e** cobalt, **f** EDX spectrum of synthesized G-CuO-Co₃O₄ hybrid nanocomposites

nanocomposite which confirms that the nanocomposite is highly pure.

HR-TEM Analysis of Graphene and G-CuO-Co₃O₄ Hybrid

Figure 5 shows the HR-TEM image of graphene nanosheets at different magnifications. Figure 5a–d clearly shows the few layers, and thin, folded, and wrinkled layered-like structure of the graphene at low and high magnifications. The HR-TEM image of the folded and transparent 2D graphene-CuO-Co₃O₄ hybrid nanocomposites and higher magnification images are shown in Fig. 6a–g. The distribution of CuO nanorods and Co₃O₄ nanoparticle on the graphene sheets and interlayered between graphene sheets can be observed in the HR-TEM image Fig. 6e, f. At higher magnification, the presence of graphene, CuO nanorods, and Co₃O₄ nanoparticle layered structures is marked with a dotted circle in Fig. 6e, f. Furthermore, the higher magnification image demonstrates the crystalline nature of the CuO nanorods and Co₃O₄ nanoparticles, as observed by the lattice fringes with clear d spacing and amorphous graphene characteristics. In Fig. 6f, g, the lattice fringe pattern

of CuO nanorods and Co₃O₄ nanoparticles are visible, and the calculated lattice fringe width is 0.30 nm. The lattice fringe pattern for other orientations of CuO nanorods and Co₃O₄ nanoparticles and graphene are also confirmed in Fig. 6f, g. The size of the CuO nanorods and Co₃O₄ nanoparticles were measured as 100–50 and 5–2 nm, respectively. Figure 6 h shows the corresponding SAED pattern of G-CuO-Co₃O₄ hybrid nanocomposites, which contains both continuous circles and a bright spot. The bright spots are due to the presence of highly polycrystalline CuO nanorods and Co₃O₄ nanoparticles in the graphene sheets, represented by the continuous circle in the SAED pattern. The CuO nanorods and Co₃O₄ nanoparticles were chemically attached to the graphene surface. These HR-TEM images provide clear evidence for hybrid nanocomposite formation.

FT-IR Spectra

The presence of various functional groups in the synthesized graphene oxide and G-CuO-Co₃O₄ hybrid nanocomposite was analysed using FTIR spectra. Figure 7a shows the FTIR spectrum with a large number of

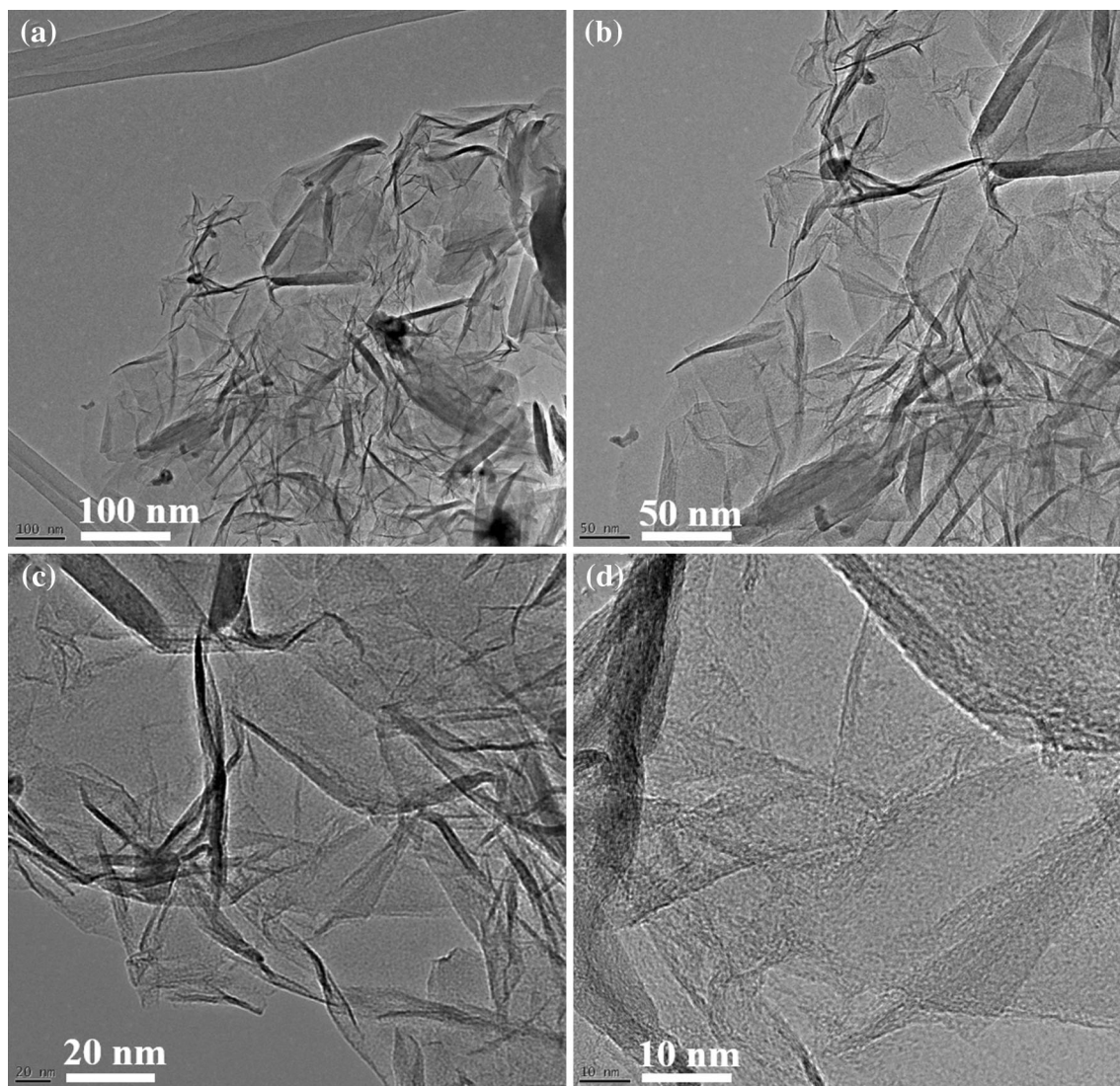


Fig. 5 HR-TEM image of graphene under different magnifications

functional groups. A broad peak corresponding to the O–H group in water molecules appears at 3214 cm^{-1} . The same functional group has been strongly reduced in the G–CuO– Co_3O_4 hybrid nanocomposite, as shown in Fig. 7b. The vibrational modes, such as $\text{C}\equiv\text{C}$, $\text{C}=\text{C}$, and aromatic nitro compounds, appear at 2121 , 1653 and 1539 cm^{-1} , respectively, and are associated with the formation of graphene.

The presence of a $\text{C}=\text{C}$ strong vibrational peak implies the formation of hexagonal structure of graphene oxide (GO) and graphene. The previously described functional groups were completely suppressed, which confirms the formation of graphene nanocomposites, as shown in Fig. 7b. It also confirms the successful reduction of GO to graphene. Similarly, for the G–CuO– Co_3O_4 hybrid nanocomposite, the intensity of the vibrational peaks decreased and were shifted to lower wavenumbers

compared to GO (Fig. 7a). The peak at 593 and 499 cm^{-1} confirms the metal oxygen bond (Cu–O) associated with CuO nanorods, and the peak at 427 cm^{-1} represents the O–Co–O bond in the nanocomposite. Thus, the FTIR results confirm the formation of the G–CuO– Co_3O_4 hybrid nanocomposite.

XPS Spectra Analysis of Hybrid Nanocomposite

Figure 8 shows the XPS spectra of the G–CuO– Co_3O_4 hybrid nanocomposite. The binding states of chemical composition and metal oxidation state CuO nanorods and Co_3O_4 nanoparticles embedded in the graphene sheets are elucidated using XPS. The survey spectrum (Fig. 8a) shows the presence of all elements in the hybrid nanocomposite. The C 1s spectrum, Fig. 8b, contains a peak at 284.38 eV due to the binding state of graphitic

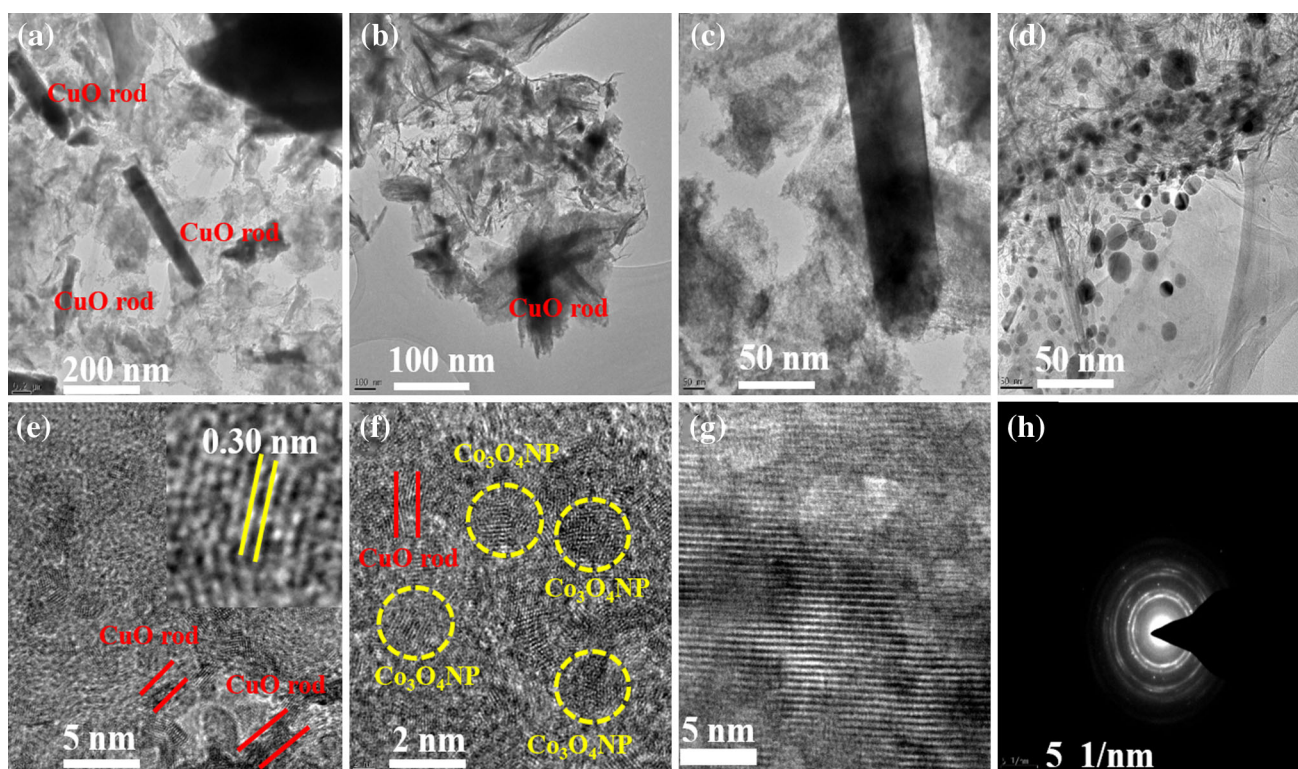


Fig. 6 a–g HR-TEM images of G–CuO–Co₃O₄ hybrid nanocomposites under different magnifications. **f** SAED patterns for the corresponding hybrid nanocomposites

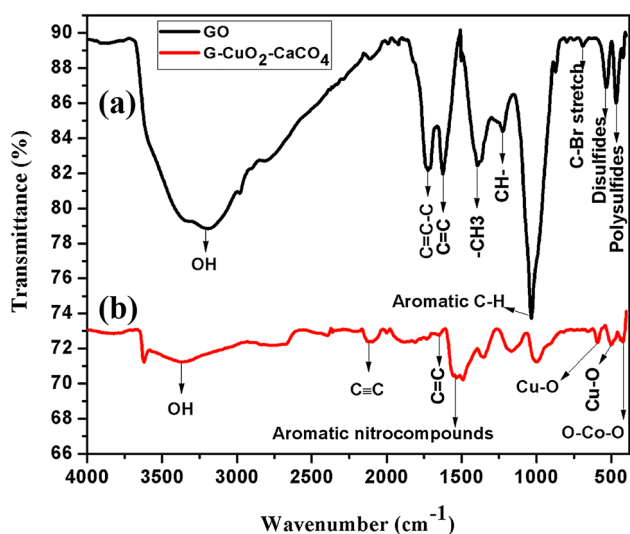


Fig. 7 FT-IR spectra of graphene oxide and G–CuO–Co₃O₄ hybrid nanocomposites

carbon, C=C, in the nanocomposite. Figure 8c shows the spectrum for the O 1s electron spectrum of oxygen, which has a peak at the binding energy of 531.59 eV. The 531.59 eV peak has been assigned to the oxygen in the carboxyl and hydroxyl groups of graphene [62]. The core level spectrum for Co 2p shown in Fig. 8d reveals the binding state of 2p electrons of Co at 781.08 and

797.13 eV, corresponding to Co 2p_{3/2} and Co 2p_{1/2}, respectively. These are in good agreement with the binding energy values for Co in a Co₃O₄ pure cubic structure [55] with spin orbit splitting at 16.05 eV.

The core level spectrum of Cu 2p shown in Fig. 8e reveals that the 2p electron binding state of Cu at 932.41 eV and 952.29 eV, corresponding to Cu 2p_{3/2} and Cu 2p_{1/2}, respectively. These are in good agreement with the binding energy value of CuO for the monoclinic phase structure (Datasheet of American Elements' catalog) [13]. The reduced GO has residual functional groups, such as OH and COOH, on the surface, which can form strong chemical bonding with CuO nanorods and Co₃O₄ nanoparticles. The XPS results also confirm the formation of the hybrid nanocomposites.

Raman Spectral Analyses of the G–CuO–Co₃O₄ Hybrid Nanocomposites

The Raman spectra of graphene, and G–CuO–Co₃O₄ hybrid nanocomposite were recorded in the 200–1800 cm⁻¹ range, as shown in Fig. 9. The Raman spectroscopy measurements were conducted at room temperature to characterize the carbonaceous materials. In particular, the measurements were used to distinguish the order and disorder of crystal structures and monitor minor

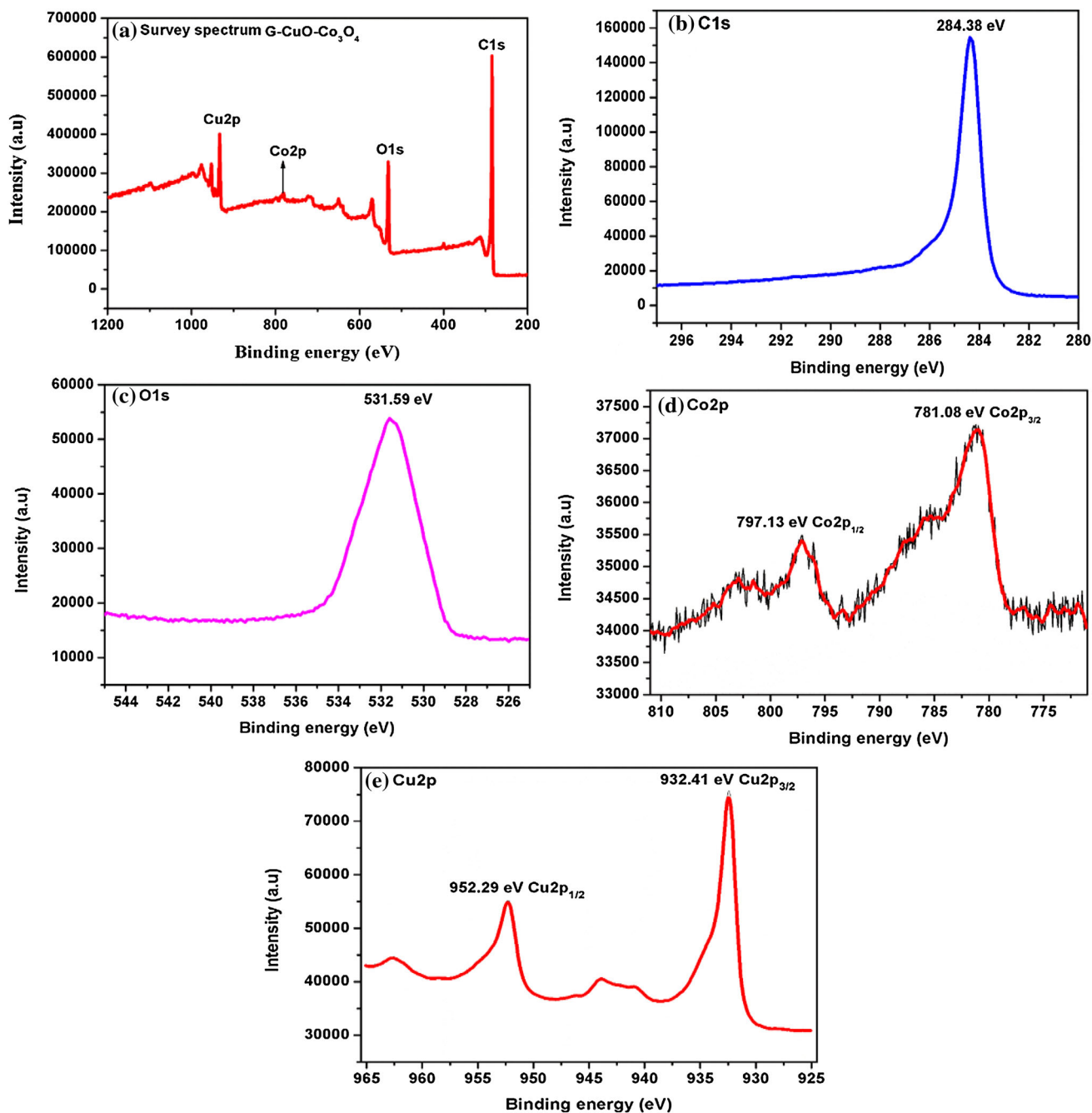


Fig. 8 Core level XPS spectrum of the G-CuO-Co₃O₄ hybrid nanocomposites **a** survey spectrum, **b** C 1s spectrum of carbon, **c** O 1s electron spectrum of oxygen, **d** Co 2p of Co₃O₄ nanoparticles, **e** Cu 2p CuO nanorods

changes inside the carbon layers and nanocomposites. Figure 9 shows the Raman spectrum for graphene; the Stokes phonon energy shift and laser excitation created two main band structures. The band at 1322.20 cm^{-1} is a primary in-plane vibrational mode of the D band. The second-order overtone of a different in-plane vibration of sp^2 hybridization of the carbon atom in the graphene sheet is observed at 1573.84 cm^{-1} , which is called the G-band [59]. The two bands indicate that the D-band has an edge

disordered k-point phonon band structure with A_{1g} symmetry carbon atoms. The G-band shows an E_{2g} mode of order band structure for carbon atom sp^2 hybridization [52]. The disordered nature of graphene increases as the Raman intensity increases [44]. The graphene peaks are observed at 1594.49 cm^{-1} (G-band) and 1352.15 cm^{-1} (D-band). From the Raman spectra, the defects were related to the I_D/I_G ratio and, the intensity of the peaks. For the G-CuO-Co₃O₄ hybrid nanocomposite, the ratio was

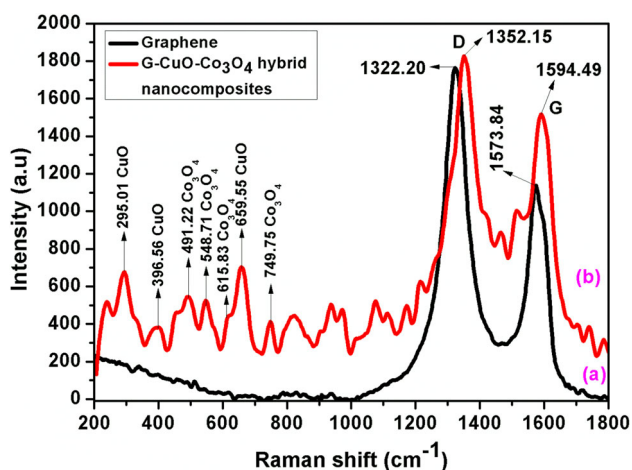


Fig. 9 Raman spectra of G–CuO–Co₃O₄ hybrid nanocomposites

calculated as 0.85, which indicates that the nanocomposite had few defects. The Raman spectrum of the G–CuO–Co₃O₄ hybrid nanocomposite revealed that the CuO nanorods are attached to the graphene sheets. The peaks at 295.01, 396.56 and 659.55 cm⁻¹ are related to the distinct vibrational modes of the monoclinic phase structure of CuO nanorods corresponding to the 295.01 (A_g), 396.56 (B_g⁽¹⁾), and 659.55 cm⁻¹ (B_g⁽²⁾) modes of CuO crystals [11]. The Co₃O₄ nanoparticles are also attached to the graphene sheets, with peaks at 491.22, 548.71, 615.83 and 749.75 cm⁻¹. The peaks at 491.22 and 548.71 cm⁻¹ were attributed to the F_{2g} mode of vibration and the peaks at 615.83 and 749.75 cm⁻¹ were assigned to the E_g and A_{1g} modes of vibrations, respectively [43, 59]. From the Raman spectrum, the CuO nanorods and Co₃O₄ nanoparticles are clearly observable in the formation of the as-synthesized hybrid nanocomposites. The hybrid nanocomposite CuO nanorod and Co₃O₄ nanoparticle graphene peaks shifted towards higher wave numbers due to the inclusion of metal oxide in the hybrid nanocomposites. The purity and composition of CuO and Co₃O₄ nanoparticles were further confirmed from the XPS spectra in Fig. 6. The Raman spectra results confirm the formation of the hybrid nanocomposites.

Visible Light Photocatalytic Activity of G–CuO–Co₃O₄ Hybrid Nanocomposites

The photocatalytic activity of the synthesized G–CuO–Co₃O₄ hybrid nanocomposite was studied on anionic dyes using MO, CR, and industrial influent and effluent dye degradation using visible light irradiation, as shown in Fig. 10. The time dependent irradiation absorption spectrum plotted as time versus C/C₀ of visible light for different time intervals and the degradation rates for MO and

CR dyes are shown in Fig. 10a–c. These results clearly show that visible light irradiated MO and CR dyes with G–CuO–Co₃O₄ hybrid nanocomposite quickly degraded within 15 min. Based on absorbance, the colour of the MO and CR dyes with G–CuO–Co₃O₄ hybrid nanocomposite decreased with increasing irradiation time. Complete colour removal was achieved with 15 min of irradiation, and the resultant degradation efficiency for MO and CR dyes was 99.85 and 99.50%, respectively, as shown in Fig. 10c. Figure 10b, d shows the time dependent absorption spectra plotted as time versus C/C₀, and the degradation efficiency of industrial effluent and Influent dye solutions with G–CuO–Co₃O₄ hybrid nanocomposite under visible light irradiation for different time intervals. Figure 10b shows that the effluent dye degraded rapidly after 60 min, while the influent dye degraded slowly, even after 300 min under visible light irradiation. The industrial dyes incorporate the sum of the residual compounds. The pollutant contamination characteristics that accompany the dyeing industry are primarily due to the non-biodegradable nature of the dyes [14]; the effluents contain appreciable amounts of toxic trace metals, acids, alkalis, and carcinogenic aromatic amines [34]. Figure 10d shows the relationship between irradiation time and degradation efficiency in % for the effluent and influent dyes after visible light irradiation: 86.23% of effluent dye was removed after 60 min of visible light irradiation and 68.45% of influent dye was removed after 300 min of visible light irradiation.

To demonstrate the influence of graphene on photodegradation, the degradation of MO, CR, and effluent and influent dye was studied under visible light. Figure 10a, b shows the variation in C/C₀ with irradiated time for G–CuO–Co₃O₄ hybrid nanocomposite, where C₀ is the initial concentration of the dye solution, and C is the concentration of the dye solution with respect to the degradation time *t*. It is clear from Fig. 10c, d that the rate of degradation was faster in the synthesized hybrid nanocomposite, which shows the beneficial impact of graphene on the photocatalytic performance of the composite.

Recycling of the photocatalyst is important for practical photocatalytic dye degradation applications. The efficiencies of the synthesized G–CuO–Co₃O₄ hybrid nanocomposites were evaluated; the photodegradation of the MO, CR, effluent and influent dyes was measured for three cycles of visible light irradiation. The decolouration periods of the MO, CR, effluent, and influent dyes for the three cycles are compared in Fig. 11a. The degradation efficiency on the dyes decreased over the course of the three recycling tests. However, it was not significant enough to impede the photocatalytic activity, which showed good repeatability. Therefore, the results showed the important cycling stability of G–CuO–Co₃O₄ hybrid nanocomposites as catalysts.

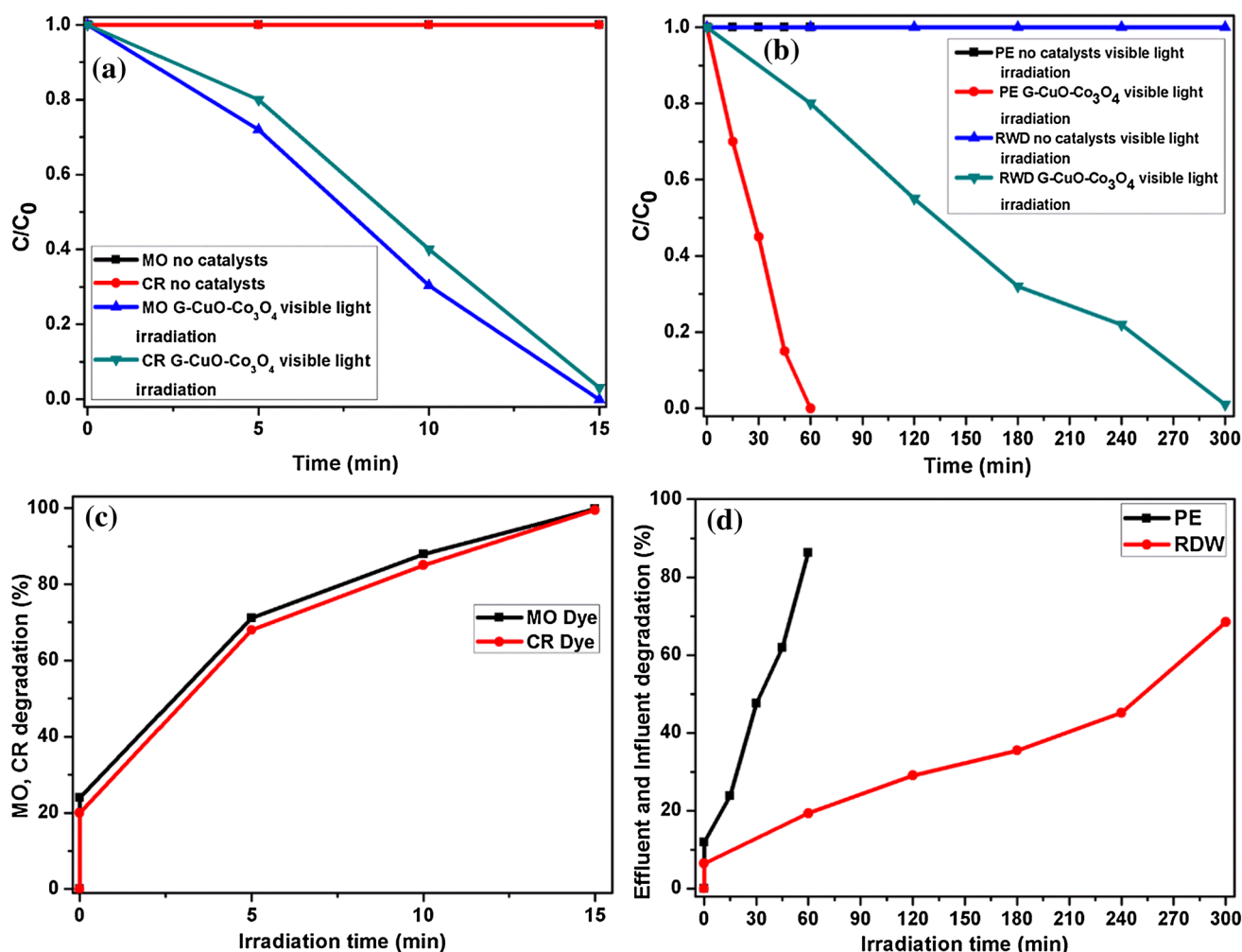


Fig. 10 Photodegradation of the MO and CR synthetic dyes and the RDW and PE industrial wastewater dyes from visible light irradiation. **a, b** C/C₀ versus time in min for the G-CuO-Co₃O₄ hybrid

nanocomposites. **c, d** Irradiation time versus dye degradation in %. PHOTO LAMP (steel light) SMC 220V-55W E26 5400 K visible light source for photocatalytic irradiation processing

The Langmuir–Hinshelwood model [20] can describe the relationships between irradiation time and the rates of photocatalytic degradation of MO, CR, effluent and influent dyes in the presence of G-CuO-Co₃O₄ hybrid nanocomposites. The reaction rate constant is calculated from Eq. (1) [48]:

$$-dC/dt = kL - HK_{ad} C/1 + K_{ad} C \tag{1}$$

where K_{ad} is the adsorption coefficient of the reactant on the G-CuO-Co₃O₄ hybrid nanocomposites, $kL - H$ is the reaction rate constant and C is the concentration at any time t . The $kL - H$ and K_{ad} terms represent the influence of light intensity on the equilibrium constant for the fast adsorption and desorption behaviour between the surface monolayer of the G-CuO-Co₃O₄ hybrid nanocomposites.

Equation (1) is integrated in the following form:

$$\ln(C/C_0) = K(C - C_0) + kL - HK_{ad}t \tag{2}$$

where C_0 is the initial concentration. Therefore, the pseudo-first-order reaction $K_{ad} C$ is very small and the equation can be shortened and integrated as follows:

$$\ln(C/C_0) = kL - HK_{ad}t = kt \tag{3}$$

where $k = kL - H K_{ad}$ is the pseudo-first-order reaction rate constant, and the half-life $t_{(1/2)}$ can be calculated as follows:

$$t_{(1/2)} = \ln 2/k \tag{4}$$

Plotting the natural logarithm of the absorption after photocatalytic degradation, i.e., $\ln(C/C_0)$, as a function of the resultant irradiation time in min reveals a linear relationship, as shown in Fig. 11b, c. Therefore, the photocatalytic degradation reaction of the MO, CR, and effluent and influent dyes with the G-CuO-Co₃O₄ hybrid

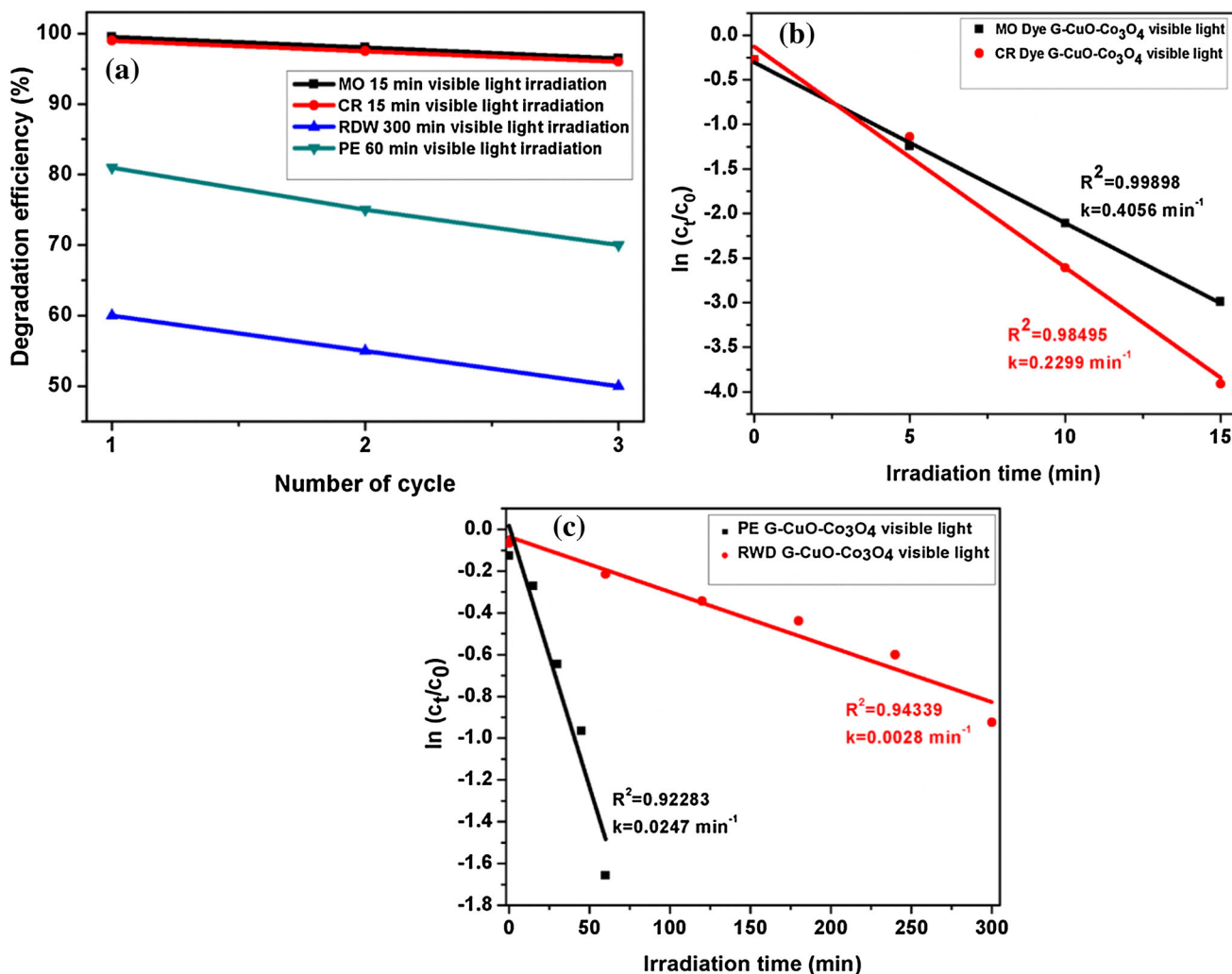


Fig. 11 a The recycling effect on photocatalytic dye degradation for various dyes in the presence of G–CuO–Co₃O₄ hybrid nanocomposites under visible light irradiation. b The first order kinetic plot for the

MO and CR synthetic dyes. c The first order kinetic plot for the RDW and PE industrial wastewater dyes

nanocomposites follows a pseudo-first-order kinetics relationship. The rate constant is the slope of the straight line in Fig. 11b, c. Equation (4) was used to determine the half-life of the photocatalytic degradation of MO, CR, and effluent and influent dyes with the G–CuO–Co₃O₄ hybrid nanocomposites. These values are summarized in Table 1. The rate constant of the degradation reaction was relatively higher and the reaction half-life decreased under visible

light; therefore, visible light produced faster dye degradation.

Colour and COD Removal

Figure 12a–d presents the colour degradation and COD removal percentages (%) of MO and CR anionic dyes and effluent and influent industrial textile dyes under visible

Table 1 Comparison of rate constants and reaction half-lives for different dyes under visible light irradiation

S. no	Irradiation sources	Dye sources	Rate constant (k) (min ⁻¹)	T _(1/2) (min ⁻¹)
1	Visible light	MO	0.4056	1.7089
2		CR	0.2299	3.0149
3		RDW	0.0247	28.0626
4		PE	0.0028	247.5526

MO methyl orange, CR Congo red, RDW raw dye wastewater, PE primary effluent

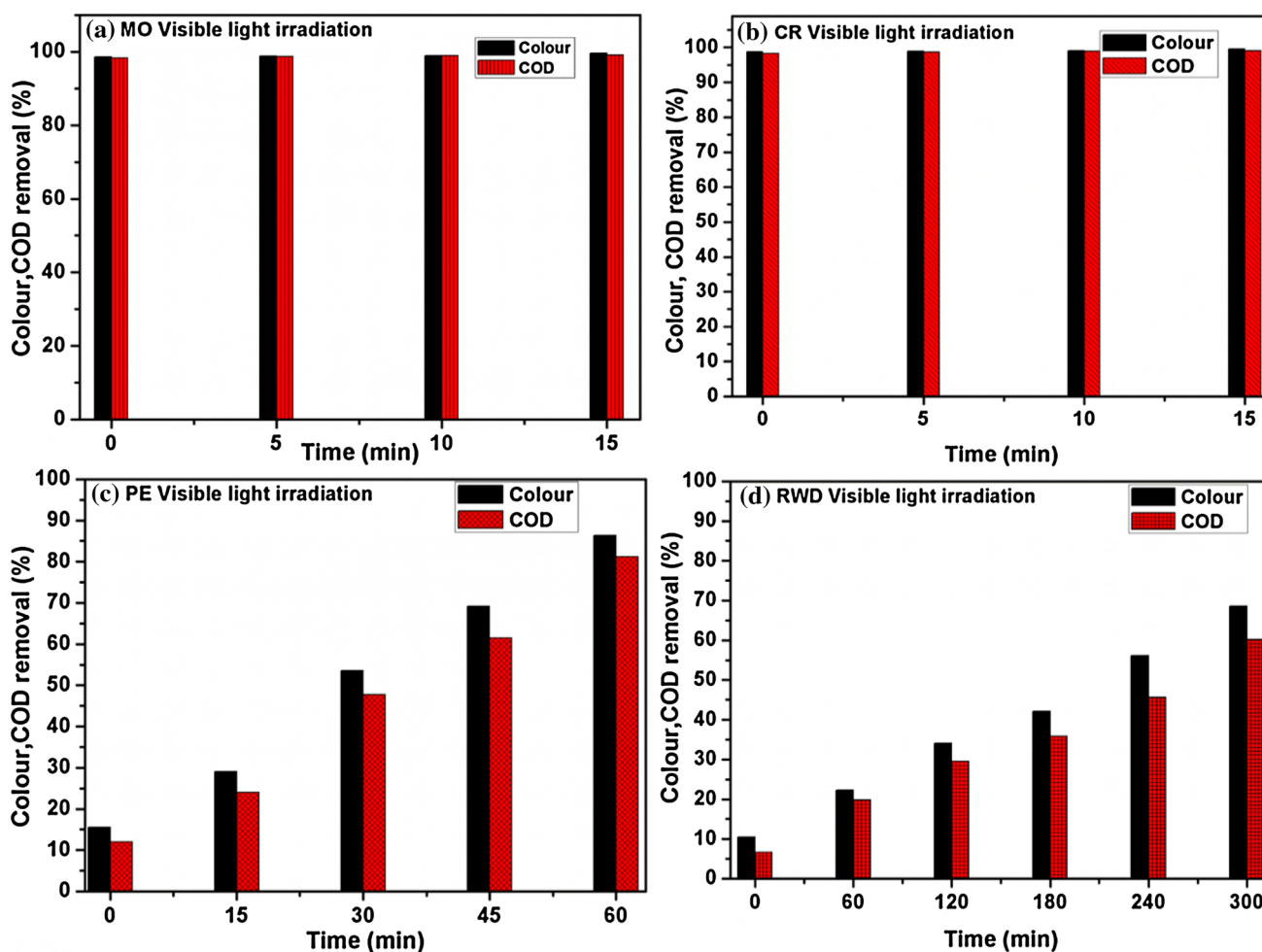


Fig. 12 COD removal of **a**, **b** the MO and CR synthetic dyes, **c**, **d** RDW and PE industrial wastewater dyes

light irradiation. The addition of the G–CuO–Co₃O₄ hybrid nanocomposites to the MO and CR anionic dyes respectively resulted in 99.20 and 99.16% COD removal within 15 min under visible light irradiation. The industrial textile dyes showed greater variability under visible light irradiation. After 60 min, the effluent dye with G–CuO–Co₃O₄ hybrid nanocomposites reached 81.45% COD removal. In contrast, after 300 min, the influent achieved 60.09% COD removal. The efficiency of the adsorption process for MO, CR, and effluent and influent wastewater dyes treated with G–CuO–Co₃O₄ hybrid nanocomposites were also examined based on colour. The colour removal percentages for the MO and CR dyes were 99.69 and 99.45%, respectively, and were 86.37 and 68.52% for the effluent and influent wastewater, respectively. The relationship between photocatalytic activity and irradiation time is illustrated in Fig. 12.

From the graph, increasing irradiation time results in a gradual decrease in colour and COD values. Generally, significant COD and colour removal from the MO, CR, and effluent and influent industrial textile wastewater dyes

occurred after visible light irradiation. Therefore, the results showed that colour and COD removal were enhanced due to visible light irradiation.

Photocatalytic Dye Degradation Mechanism

The photodegradation mechanism on the dye molecule after addition of the G–CuO–Co₃O₄ hybrid nanocomposites and exposure to visible light is shown in Fig. 13. The reduced graphene has several residual functional groups, e.g., hydroxyl and carboxyl groups, enriched on the surface. During light irradiation, the excitons are generated in the CuO and Co₃O₄ by absorbing the photons. The photoexcited electrons react with the residual functional groups of graphene and increase the oxide radicals (O₂^{•−}) due to the reduction process at the conduction band. Furthermore, the presence of graphene reduces the recombination of electrons and increases the reduction reaction, as it is a highly conducting medium. Concurrently, the oxidation reaction at the valence band increases the hydroxyl radicals (OH[•]), as shown in Fig. 13. The O₂^{•−} and OH[•]

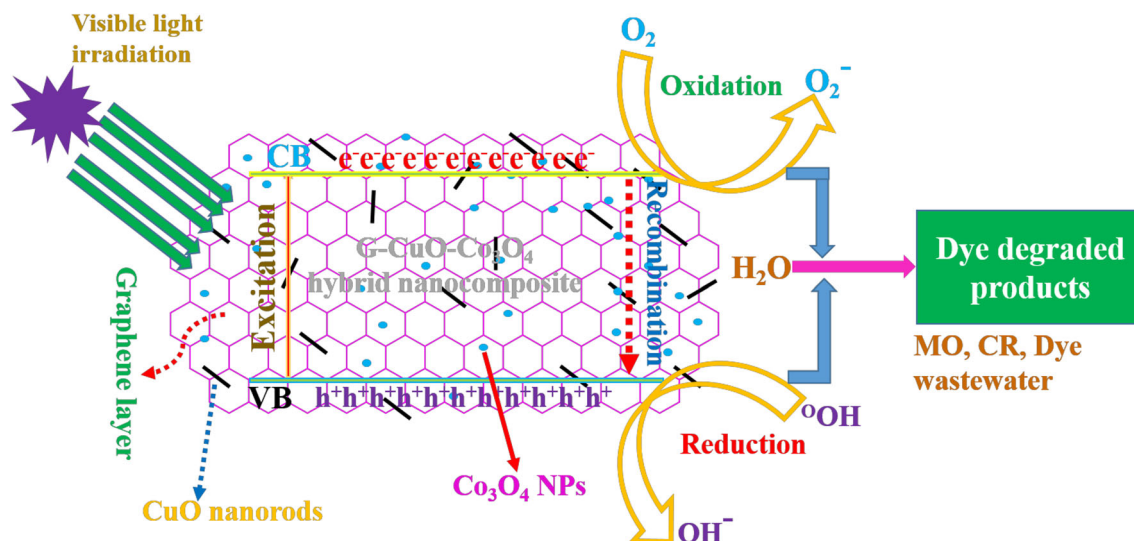


Fig. 13 Photocatalytic dye degradation mechanism for synthesized G-CuO-Co₃O₄ hybrid nanocomposites under visible light irradiation

radicals are extremely active and decompose the dye molecules with a strong reaction. Therefore, the G-CuO-Co₃O₄ hybrid nanocomposites exhibit enhanced photocatalytic activity under visible light irradiation.

Conclusions

The G-CuO-Co₃O₄ hybrid nanocomposite has been successfully synthesized using a simple and efficient in situ surfactant free hydrothermal method. The distribution and incorporation of CuO nanorods and Co₃O₄ nanoparticles on the graphene sheets and interlayer of graphene sheets was confirmed with morphology from FE-SEM and HR-TEM analyses. Structural analysis confirms the hexagonal structure of graphene, monoclinic phase of CuO nanorods, and cubic structure of Co₃O₄. XPS analysis confirmed the strong bonding of Cu and Co with graphene sheets. The degradation of synthetic anionic dyes, MO and CR, and industrial dye wastewater, raw and primary treated effluent, was studied after irradiation with visible light sources and G-CuO-Co₃O₄ hybrid nanocomposite as catalysts. The results prove that the G-CuO-Co₃O₄ hybrid nanocomposites performed as effective catalysts to degrade colour and COD with visible light sources. The photocatalytic results revealed that the synthesized hybrid nanocomposites are an effective alternative technology for potential treatment of industrial wastewater to remove dye pollutants.

Acknowledgements This research was supported by Basic Science Research Program through the National Research Foundation of Korea (NRF) funded by the Ministry of Education (2017R1D1A3B03029814).

References

1. A. A. Ahmad and B. H. Hameed (2010). Effect of preparation conditions of activated carbon from bamboo waste for real textile wastewater. *J. Hazard. Mater.* **173**, 487–493.
2. American Public Health Association (APHA) *Standard Methods for the Examination of Water and Wastewater*, 21st ed (American Public Health Association, Washington, DC, 2005).
3. R. Asahi, T. Morikawa, T. Ohwaki, K. Aoki, and Y. Taga (2001). Visible-light photocatalysis in nitrogen-doped titanium oxides. *Science* **293**, 269–271.
4. N. Azbar, T. Yonar, and K. Kestioglu (2004). Comparison of various advanced oxidation processes and chemical treatment methods for COD and color removal from a polyester and acetate fiber dyeing effluent. *Chemosphere* **55**, 35–43.
5. X. Bai, L. Wang, and Y. Zhu (2012). Visible photocatalytic activity enhancement of ZnWO₄ by graphene hybridization. *ACS Catal.* **2**, 2769–2778.
6. E. Barrera, I. Gonzalez, and T. Viveros (1998). A new cobalt oxide electrodeposit bath for solar absorbers. *Sol. Energy Mater. Sol. Cells* **51**, 69–82.
7. E. Bi, H. Chen, X. Yang, W. Peng, M. Gratzel, and L. Han (2014). A quasi core-shell nitrogen-doped graphene/cobalt sulfide conductive catalyst for highly efficient dye-sensitized solar cells. *Energy Environ. Sci.* **7**, 2637–2641.
8. Y. Bu, Z. Chen, W. Li, and B. Hou (2013). Highly efficient photocatalytic performance of graphene-ZnO quasi-shell-core composite material. *ACS Appl. Mater. Interfaces* **5**, 12361–12368.
9. O. T. Can, M. Kobya, E. Demirbas, and M. Bayramoglu (2006). Treatment of the textile wastewater by combined electrocoagulation. *Chemosphere* **62**, 181–187.
10. H. Chen, G. Jhao, and Y. Liu (2013). Low-temperature solution synthesis of CuO nanorods with thin diameter. *Mater. Lett.* **93**, 60–63.
11. X. K. Chen, J. C. Irwin, and J. P. Franck (1995). Evidence for a strong spin-phonon interaction in cupric oxide. *Phys. Rev. B* **52**, R13130.
12. Y. S. Chen and P. V. Kamat (2014). Glutathione-capped gold nanoclusters as photosensitizers. Visible light-induced hydrogen generation in neutral water. *J. Am. Chem. Soc.* **136**, 6075–6082.

13. Datasheet of American Elements' catalog. Available <http://www.americanelements.com/copper-ii-ethoxide-2850-65-9.html>. American Elements is a US Registered Trademark. Accessed 01 Jan 1998.
14. R. S. Dave and A. R. Patel (2010). Photochemical and photocatalytic of cypermethrin under UV radiation. *Der Pharma Chem.* **2**, 152–158.
15. R. Esmaeli, A. H. Hassani, A. Eslami, M. Ahmadi Moghadam, and A. A. Safari (2011). Di-(2-Ethylhexyl) Phthalate oxidative degradation by Fenton process in synthetic and real petrochemical wastewater. *Iran. J. Environ. Health Sci. Eng.* **8**, 201–206.
16. I. Gulkaya, G. A. Surucu, and F. B. Dilek (2006). Importance of H_2O_2/Fe^{2+} ratio in Fenton's treatment of a carpet dyeing wastewater. *J. Hazard. Mater.* **136**, 763–769.
17. H. A. E. Hagelin-Weaver, G. B. Hoflund, D. M. Minahan, and G. N. Salaita (2004). Electron energy loss spectroscopic investigation of Co metal, CoO, and Co_3O_4 before and after Ar + bombardment. *Appl. Surf. Sci.* **235**, 420–448.
18. L. He, L. Jing, Y. Luan, L. Wang, and H. Fu (2014). Enhanced visible activities of $\alpha-Fe_2O_3$ by coupling N-doped graphene and mechanism insight. *ACS Catal.* **4**, 990–998.
19. M. R. Hoffman, S. T. Martin, W. Choi, and D. W. Bahnemann (1995). Environmental applications of semiconductor photocatalysis. *Chem. Rev.* **95**, 69–96.
20. A. Houas, H. Lachheb, M. Ksibi, E. Elaloui, C. Guillard, and J. Herrmann (2001). Photocatalytic degradation pathway of methylene blue in water. *Appl. Catal. B* **31**, 145–157.
21. Y. W. Kang, M. J. Cho, and K. Y. Hwang (1999). Correction of hydrogen peroxide interference on standard chemical oxygen demand test. *Water Res.* **33**, 1247–1251.
22. V. Kavitha and K. Palanivelu (2005). Destruction of cresols by Fenton oxidation process. *Water Res.* **39**, 3062–3072.
23. M. Kobya, O. T. Can, and M. Bayramoglu (2003). Treatment of textile wastewaters by electrocoagulation using iron and aluminum electrodes. *J. Hazard. Mater.* **100**, 163–178.
24. S. Kohtani, J. Hiro, N. Yamamoto, A. Kudo, K. Tokumura, and R. Nakagaki (2005). Adsorptive and photocatalytic properties of Ag-loaded $BiVO_4$ on the degradation of 4-*n*-alkylphenols under visible light irradiation. *Catal. Commun.* **6**, 185–189.
25. S. Kohtani, M. Koshiko, A. Kudo, K. Tokumura, Y. Ishigaki, A. Toriba, K. Hayakawa, and R. Nakagaki (2003). Photodegradation of 4-alkylphenols using $BiVO_4$ photocatalyst under irradiation with visible light from a solar simulator. *Appl. Catal. B* **46**, 573–586.
26. K. Krishnamoorthy, R. Mohan, and S. J. Kim (2011). Graphene oxide as a photocatalyst material. *Appl. Phys. Lett.* **98**, 1–3.
27. A. Kudo, H. Kato, and I. Tsuji (2004). Strategies for the development of visible-light driven photo catalysts for water splitting. *Chem. Lett.* **33**, 1534–1539.
28. M. R. Kumar (2009). Recycling of woven fabric dyeing wastewater practiced in Perundurai common effluent treatment plant. *Mod. Appl. Sci.* **3**, 146–160.
29. R. Leary and A. Westwood (2011). Carbonaceous nanomaterials for the enhancement of TiO_2 photocatalysis. *Carbon* **49**, 741–772.
30. J. Lee, D. H. K. Jackson, T. Li, R. E. Winans, J. A. Dumesic, T. F. Kuech, and G. W. Huber (2014). Enhanced stability of cobalt catalysts by atomic layer deposition for aqueous-phase reactions. *Energy Environ. Sci.* **7**, 1657–1660.
31. H. Liang, J. M. Raitano, L. Zhang, and S. W. Chan (2009). Controlled synthesis of Co_3O_4 nanopolyhedrons and nanosheets at low temperature. *Chem. Commun.*, 7569–7571.
32. H. M. Liu, R. Nakamura, and Y. Nakato (2005). Bismuth-copper vanadate $BiCu_2VO_6$ as a novel photocatalyst for efficient visible-light-driven oxygen evolution. *Chem. Phys. Chem.* **6**, 2499–2502.
33. M. Liu, R. Inde, M. Nishikawa, X. Qiu, D. Atarashi, E. Sakai, Y. Nosaka, K. Hashimoto, and M. Miyauchi (2014). Enhanced photoactivity with nanocluster-grafted titanium dioxide photocatalysts. *ACS Nano* **8**, 7229–7238.
34. N. Manivasakam *Industrial Effluents Origin, Characteristics, Effects, Analysis and Treatment* (Sakthi Publications, Coimbatore, 2003).
35. L. Metcalf and H. P. Eddy *Wastewater Engineering: Treatment and Reuse*, 4th ed (McGraw-Hill, New York, 2004), pp. 93–94.
36. M. Niu, D. Cheng, and D. Cao (2014). Understanding the mechanism of photocatalysis enhancements in the graphene-like semiconductor sheet/ TiO_2 composites. *J. Phys. Chem. C* **118**, 5954–5960.
37. M. Panizza and M. A. Oturan (2011). Degradation of Alizarin Red by electro-Fenton process using a graphite-felt cathode. *Electrochim. Acta* **56**, 7084–7087.
38. S. K. Pardeshi and A. B. Patil (2008). A simple route for photocatalytic degradation of phenol in aqueous zinc oxide suspension using solar energy. *Sol. Energy* **82**, 700–705.
39. K. M. Parida and S. Parija (2006). Photocatalytic degradation of phenol under solar radiation using microwave irradiated zinc oxide. *Sol. Energy* **80**, 1048–1054.
40. P. S. Patil, L. D. Kadam, and C. D. Lokhande (1996). Preparation and characterization of spray pyrolysed cobalt oxide thin films. *Thin Solid Films* **272**, 29–32.
41. Pham TA, Kim J, Kim JS, Jeong YT, Corrigendum to (2011) "One-step reduction of graphene oxide with L-glutathione" [*Colloids Surf. A: Physicochem. Eng. Asp.* **384**, 543–548], *Colloids Surf. A Physicochem. Eng. Asp.* **384**, 543.
42. J. J. Pignatello, E. Oliveros, and A. Mackay (2006). Advanced oxidation processes for organic contaminant destruction based on the Fenton reaction and related chemistry. *J. Crit. Rev. Environ. Sci. Technol.* **36**, 1–84.
43. W. H. Ryu, T. H. Yoon, S. H. Song, S. Jeon, Y. J. Park, and I. D. Kim (2013). Bifunctional composite catalysts using Co_3O_4 nanofibers immobilized on nonoxidized graphene nanoflakes for high-capacity and long-cycle-Li- O_2 batteries. *Nano Lett.* **13**, 4190–4197.
44. R. Saito, M. Hofmann, G. Dresselhaus, A. Jorio, and M. S. Dresselhaus (2011). Raman spectroscopy of graphene and carbon nanotubes. *Adv. Phys.* **60**, 413–550.
45. S. Sakthivel and H. Kisch (2003). Daylight photocatalysis by carbon-modified titanium dioxide. *Angew. Chem. Int. Ed.* **42**, 4908–4911.
46. M. Shanmugam and R. Jayavel (2015). Synthesize of graphene-tin oxide nanocomposite and its photocatalytic properties for the degradation of organic pollutants under visible light. *J. Nanosci. Nanotechnol.* **15**, 7195–7201.
47. K. M. Srestha, C. M. Sorensen, and K. J. Klabunde (2010). Synthesis of CuO nanorods, reduction of CuO into Cu nanorods, and diffuse reflectance measurements of CuO and Cu nanomaterials in the near infrared region. *J. Phys. Chem. C* **114**, 14368–14376.
48. Z. Sun, Y. Chen, Q. Ke, Y. Yang, and J. Yuan (2002). Photocatalytic degradation of a cationic azo dye by TiO_2 /bentonite nanocomposite. *J. Photochem. Photobiol. A* **149**, 169–174.
49. L. L. Tan, W. J. Ong, S. P. Chai, and A. R. Mohamed (2015). Noble metal modified reduced graphene oxide/ TiO_2 ternary nanostructures for efficient visible-light-driven photoreduction of carbon dioxide into methane. *Appl. Catal. B Environ.* **166–167**, 251–259.
50. J. W. Tang, Z. G. Zou, and J. H. Ye (2004). Efficient photocatalytic decomposition of organic contaminants over $CaBi_2O_4$ under visible light-irradiation. *Angew. Chem. Int. Ed.* **43**, 4463–4466.

51. G. Tchobanoglous and F. L. Burton *Wastewater Engineering: Treatment, Disposal and Reuse* (Tata McGraw- Hill Publishing Co., Ltd., New Delhi, 1995).
52. F. Tuinstra and J. L. Koenig (1970). Raman spectrum of graphite. *J. Chem. Phys.* **53**, 1126–1130.
53. D. Venieri, A. Fraggadaki, M. Kostadima, E. Chatzisyneon, V. Binas, A. Zachopoulos, G. Kiriakidis, and D. Mantzavinos (2014). Solar light and metal-doped TiO₂ to eliminate water-transmitted bacterial pathogens: photocatalyst characterization and disinfection performance. *Appl. Catal. B Environ.* **154–155**, 93–101.
54. B. Weng, J. Wu, N. Zhang, and Y. J. Xu (2014). Observing the role of graphene in boosting the two-electron reduction of oxygen in graphene–WO₃ nanorod photocatalysts. *Langmuir* **30**, 5574–5584.
55. Z. S. Wu, W. C. Ren, L. Wen, L. B. Gao, J. P. Zhao, Z. P. Chen, G. M. Zhou, F. Li, and H. M. Cheng (2010). Graphene anchored with Co₃O₄ nanoparticles as anode of lithium ion batteries with enhanced reversible capacity and cyclic performance. *ACS Nano* **4**, 3187–3194.
56. Q. Xiang, J. Yu, and M. Jaroniec (2012). Graphene based semiconductor photocatalysis. *Chem. Soc. Rev.* **41**, 782–796.
57. C. Yang, X. Su, J. Wang, X. Cao, S. Wang, and L. Zhang (2013). Facile microwave-assisted hydrothermal synthesis of varied-shaped CuO nanoparticles and their gas sensing properties. *Sens. Actuators B* **185**, 159–165.
58. H. Yu, H. Irie, and K. Hashimoto (2010). Conduction band energy level control of titanium dioxide: toward an efficient visible-light-sensitive photocatalyst. *J. Am. Chem. Soc.* **132**, 6898–6899.
59. J. Yuan, J. Zhu, H. Bi, X. Meng, S. Liang, L. Zhang, and X. Wang (2013). Graphene-based 3D composite hydrogel by anchoring Co₃O₄ nanoparticles with enhanced electrochemical properties. *Phys. Chem. Chem. Phys.* **15**, 12940–12945.
60. F. Zhang, A. Yamakata, K. Maeda, Y. Moriya, T. Takata, J. Kubota, K. Teshima, S. Oishi, and K. Domen (2012). Cobalt-modified porous single-crystalline LaTiO₂N for highly efficient water oxidation under visible light. *J. Am. Chem. Soc.* **134**, 8348–8351.
61. H. Zhang, X. Chen, Z. Li, J. Kou, T. Yu, and Z. Zou (2007). Preparation of sensitized ZnS and its photocatalytic activity under visible light irradiation. *J. Phys. D Appl. Phys.* **40**, 6846–6849.
62. J. Zhang, Z. Xiong, and X. S. Zhao (2011). Graphene-metal oxide composites for the degradation of dyes under visible light irradiation. *J. Mater. Chem.* **21**, 3634–3640.
63. Y. C. Zhang, W. W. Chen, and X. Y. Hu (2007). Controllable synthesis and optical properties of Zn-doped CdS nanorods from single-source molecular precursors. *Cryst. Growth Des.* **7**, 580–586.